

A 160 μ W 8-Channel Active Electrode System for EEG Monitoring

Xu, Jiawei; Yazicioglu, Refet Firat; Grundlehner, Bernard; Harpe, Pieter; Makinwa, Kofi A.A.; Van Hoof, Chris

DOI

[10.1109/TBCAS.2011.2170985](https://doi.org/10.1109/TBCAS.2011.2170985)

Publication date

2011

Document Version

Accepted author manuscript

Published in

IEEE Transactions on Biomedical Circuits and Systems

Citation (APA)

Xu, J., Yazicioglu, R. F., Grundlehner, B., Harpe, P., Makinwa, K. A. A., & Van Hoof, C. (2011). A 160 μ W 8-Channel Active Electrode System for EEG Monitoring. *IEEE Transactions on Biomedical Circuits and Systems*, 5(6), 555-567. <https://doi.org/10.1109/TBCAS.2011.2170985>

Important note

To cite this publication, please use the final published version (if applicable).
Please check the document version above.

Copyright

Other than for strictly personal use, it is not permitted to download, forward or distribute the text or part of it, without the consent of the author(s) and/or copyright holder(s), unless the work is under an open content license such as Creative Commons.

Takedown policy

Please contact us and provide details if you believe this document breaches copyrights.
We will remove access to the work immediately and investigate your claim.

A 160 μ W 8-Channel Active Electrode System for EEG Monitoring

Jiawei Xu, Refet Firat Yazicioglu, *Member, IEEE*, Bernard Grundlehner, Pieter Harpe, Kofi A. A. Makinwa, *Fellow, IEEE*, and Chris Van Hoof, *Member, IEEE*

Abstract—This paper presents an active electrode system for gel-free biopotential EEG signal acquisition. The system consists of front-end chopper amplifiers and a back-end common-mode feedback (CMFB) circuit. The front-end AC-coupled chopper amplifier employs input impedance boosting and digitally-assisted offset trimming. The former increases the input impedance of the active electrode to 2 G Ω at 1 Hz and the latter limits the chopping induced output ripple and residual offset to 2 mV and 20 mV respectively. Thanks to chopper stabilization, the active electrode achieves 0.8 μ V_{rms} (0.5-100 Hz) input referred noise. The use of a back-end CMFB circuit further improves the CMRR of the active electrode readout to 82 dB at 50 Hz. Both front-end and back-end circuits are implemented in a 0.18 μ m CMOS process and the total current consumption of an 8-channel readout system is 88 μ A from 1.8 V supply. EEG measurements using the proposed active electrode system demonstrate its benefits compared to passive electrode systems, namely reduced sensitivity to cable motion artifacts and mains interference.

Index Terms—Active electrode, instrumentation amplifier (IA), electroencephalography (EEG), chopper modulation, input impedance, electrode offset, ripple reduction, common-mode feedback (CMFB), common-mode rejection ratio (CMRR)

I. INTRODUCTION

THERE has been a growing interest in portable biopotential monitoring systems for personalized healthcare and lifestyle applications [1]-[4]. Highly miniaturized and autonomous sensor systems (Fig. 1) enable people to access their personal body area network (BAN) for medical, sports, entertainment and brain-computer-interfaces (BCI) applications. Such systems must facilitate the recording of biopotential signals (EEG, ECG, and EMG) in a non-invasive and comfortable manner, thus enabling the exploration of various biological features and also improving patients' quality of life.



Fig. 1. IMEC's dry electrode headset for EEG monitoring.

However, one of the most important drawbacks of current ambulatory biopotential monitoring systems is the use of wet-(gel-based) electrodes. The gel dries out, which reduces signal integrity and system performance, and it also creates discomfort for the patient. Hence, the presence of gel requires continuous attention by medical professionals. These drawbacks make gel-based electrode systems unsuitable for emerging ambulatory medical applications.

One possible gel-free solution is the use of dry electrodes [5], [6]. Unfortunately, the elimination of gel elevates the electrode-tissue contact impedance (R_d in Fig. 2(a)), which increases both the level of mains interference and the severity of cable movement artifacts [7].

Manuscript received May 30, 2011; revised August 8, 2011.

J. Xu and B. Grundlehner are with IMEC/Holst Centre, High Tech Campus 31, 5656 AE Eindhoven, The Netherlands (e-mail: jiawei.xu@imec-nl.nl).

R. F. Yazicioglu and C. Van Hoof are with IMEC, 3001 Leuven, Belgium.

P. Harpe is with Eindhoven University of Technology, Eindhoven, Postbus 513, 5600 MB Eindhoven, The Netherlands.

K. A. A. Makinwa is with the Electronic Instrumentation Laboratory, Delft University of Technology, Mekelweg 4, 5628 CD Delft, The Netherlands.

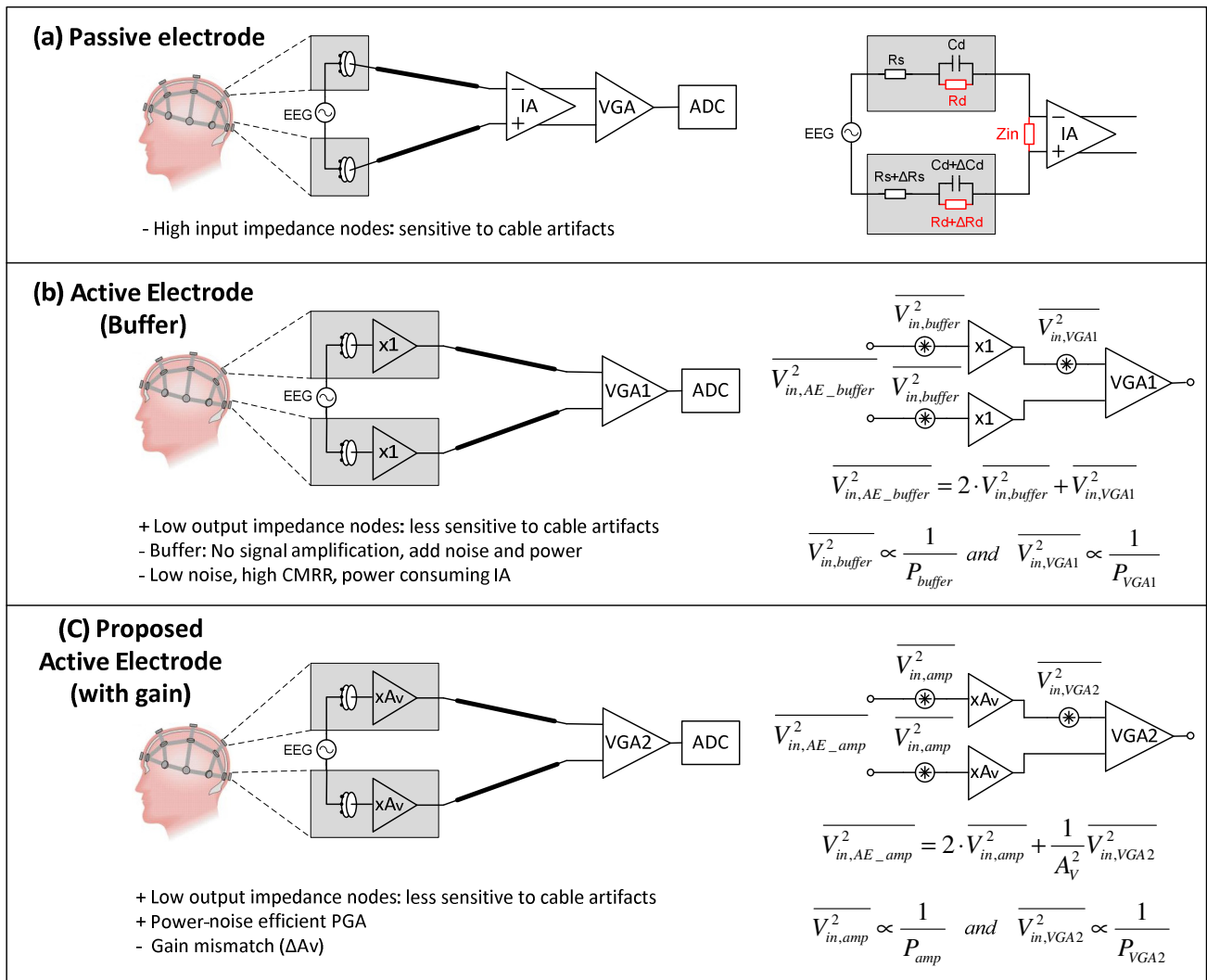


Fig. 2. Biopotential signal monitoring systems: (a) passive electrodes, (b) active electrode with buffer, and (c) active electrode with gain.

Dry electrode readout circuits are typically implemented using active electrodes [7]-[10], where a voltage buffer is co-integrated with the electrode (Fig. 2(b)). The minimal signal path between electrode and amplifier input reduces mains interference, while the low output impedance of the amplifier eliminates problems due to cable motion artifacts and 50/60 Hz interference. However, existing voltage buffers must consume a significant amount of power to meet the noise specifications. In addition, they only act as impedance converters, i.e. they do not amplify the EEG signal. Hence, a power consuming back-end instrumentation amplifier or a high-resolution ADC is still required to keep the total input referred noise at acceptable levels. Thus, the overall approach is power inefficient [11], [12].

One way to improve the power efficiency is to replace the voltage buffers by amplifiers with gain (Fig. 2(c)). The benefits of this approach are illustrated by the equivalent circuit diagrams and input referred noise expressions in Fig. 2(b)-(c),

where $\overline{V_{in,AE_buffer}^2}$ and $\overline{V_{in,AE_amp}^2}$ are the total input referred

noise voltages of active electrode systems based on buffers and amplifiers respectively, $\overline{V_{in,buffer}^2}$ and $\overline{V_{in,amp}^2}$ are the input referred noise voltages of buffer and amplifier respectively, $\overline{V_{in,VGA1}^2}$ and $\overline{V_{in,VGA2}^2}$ are the input referred noise voltages of variable gain amplifiers (VGA₁ and VGA₂) respectively, P_{VGA1} and P_{VGA2} are the power consumption of the VGA₁ and VGA₂ respectively, P_{buffer} and P_{amp} are the power consumption of the buffer and amplifier respectively, A_v is the voltage gain of the proposed active electrodes in Fig. 2(c).

The front-end buffer and amplifier have approximately equal input referred noise voltage and power consumption, as shown in (1) and (2), if they are based on the same operational amplifier.

$$\overline{V_{in,buffer}^2} \approx \overline{V_{in,amp}^2} \quad (1)$$

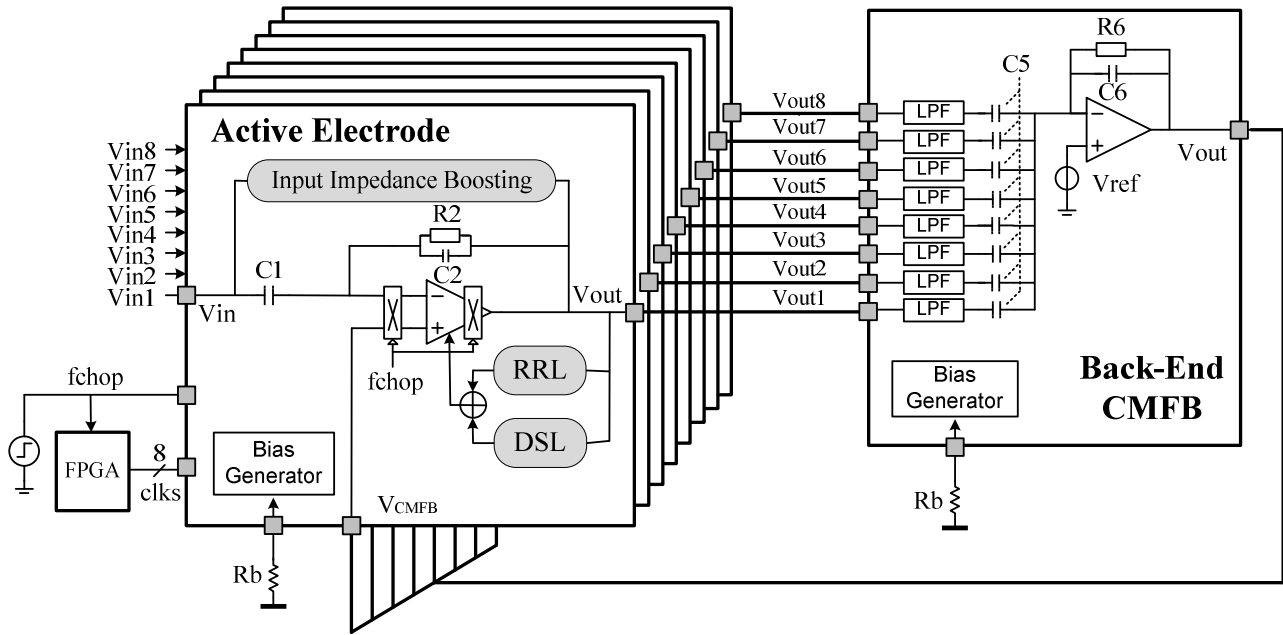


Fig. 3. Block diagram of active electrode system.

$$P_{buffer} \approx P_{amp} \quad (2)$$

The following design specification (3) is valid, when both systems target the same total input referred noise voltage.

$$\overline{V_{in,AE_buffer}^2} = \overline{V_{in,AE_amp}^2} \quad (3)$$

As a result, the noise specification of the VGA_1 in Fig. 2(c) is more relaxed than that of the VGA_2 in Fig. 2(b). Therefore, the active electrode system in Fig. 2(c) has higher noise-power efficiency because of the significantly less power consumed by the VGA, as shown in (4).

$$P_{VGA2} \approx \frac{P_{VGA1}}{A_v^2} \quad (4)$$

Previous work on active electrodes with amplification, but implemented with off-shelf components, has demonstrated high-quality recording of biopotential signals [13], [14]. However, in order to further optimize the size and power optimization of such electrodes, custom ASICs are necessary.

Unfortunately, state-of-the-art biopotential instrumentation amplifiers are not well suited for use in active electrodes intended for gel-free applications. Topologies that do not use chopper modulation suffer from $1/f$ noise [15], [16], while their CMRR is usually limited by components mismatch [17], [18]. Chopper-stabilized capacitively-coupled amplifiers [19]-[21] modulate the input signal before applying it to their input capacitors and so attenuate $1/f$ noise and increase CMRR. However, the switched-capacitor impedance formed by the input choppers and the input capacitors reduces their input

impedance. Relocating the input chopper to the virtual ground, inside the feedback loop, solves this impedance problem at the expense of reduced CMRR [21], which is now limited by capacitor mismatch. A chopper-stabilized current feedback amplifier [23] with voltage follower inputs achieves a good balance between input impedance, noise, and CMRR, but its DC servo loop limits the maximum electrode offset rejection capability to a few tens of mV. In summary, the main challenge of a gel-free active electrode system is how to design ultra-low-power instrumentation amplifiers achieving low input referred noise (50 nV/sqrt(Hz) or 0.5 μ Vrms from 0.5-100Hz), high input impedance (>100 M Ω), and high CMRR (110 dB), while extracting μ V level biopotential signals superimposed on large DC electrode polarization voltages [24].

This paper proposes an 8-channel active electrode system [25], which advances the state-of-the-art, with low input referred noise, high input impedance, rail-to-rail electrode offset rejection, as well as improved CMRR with respect to [16]-[18], [21]. Moreover, this is the first low-power gain-programmable active electrode ASIC for gel-free non-clinical EEG monitoring applications.

The paper is organized as follows: Section II describes the design details of the 8-channel active electrode system, including front-end amplifier and the back-end CMFB amplifier. Section III presents the circuit characterization results and EEG measurement results. Section IV concludes the paper.

II. ACTIVE ELECTRODE SYSTEM

A. Proposed Active Electrode System Architecture

The proposed system (Fig. 3) consists of eight front-end active electrodes based on eight chopper instrumentation amplifiers, and one back-end voltage-summing amplifier.

The front-end circuits are responsible for the high quality pre-amplification of EEG signals. The proposed active electrode (Fig. 3) is based on a AC-coupled capacitive feedback amplifier with chopper modulation at the virtual ground to suppress the amplifier's $1/f$ noise [21], in addition, the active electrode also utilizes an input-impedance boosting loop to further increase the input impedance, as well as a ripple reduction loop (RRL) and a DC servo loop (DSL) to compensate the non-idealities of the core amplifier.

The back-end summing amplifier is responsible for improving the CMRR of the proposed active electrode system, which would otherwise be limited by components mismatch (Fig. 2(c)). This back-end amplifier feeds the average common-mode (CM) voltage of all eight amplifiers back-to their non-inverting inputs (V_{CMFB}), and thus reduces the effective CM gain of these amplifiers and boosts the CMRR between electrode pairs (see Section II.C).

B. Front-End Active Electrode

The front-end active electrode consists of an AC-coupled chopper amplifier, an input-impedance boosting loop, and two offset trimming loops. The chopper amplifier's (Fig. 3) midband gain depends on the ratio of the feedback capacitors C_1/C_2 [15]. Variable gains (3, 10, 50 and 100) can be realized by switching between different values of C_2 . The back-to-back connected pseudo-resistor R_2 [26] and capacitor C_2 determine the high-pass corner of the active electrode. The AC coupling capacitor C_1 rejects the electrode offset voltage, thus avoiding amplifier saturation.

The detailed operations of the core amplifier, the offset trimming loops (RRL and DSL), and the impedance boosting loop are discussed in section B. 1), B. 2), and B. 3) respectively.

1) Core Amplifier

The core amplifier (Fig. 4) is designed for low noise, low offset and large output voltage swing. To achieve these, it consists of a low noise chopper folded-cascode amplifier, similar to the one described in [27], and two additional pairs of auxiliary current DACs (CA_1 - CA_4) for offset trimming.

The folded-cascode topology provides a good balance between output voltage swing and power consumption [28]. Having a large output voltage swing makes the amplifier robust to (large) input motion artifacts and interference.

Chopper modulation is applied to reduce the $1/f$ noise of the core amplifier. The input modulator is placed before the input transistors M_1 and M_2 , up-modulating the amplifier's input signals without affecting its input offset V_{off} . The output modulation is performed at the low impedance nodes before the dominant pole (at V_{out}), such that the bandwidth of the amplifier does not limit the chopping frequency [27].

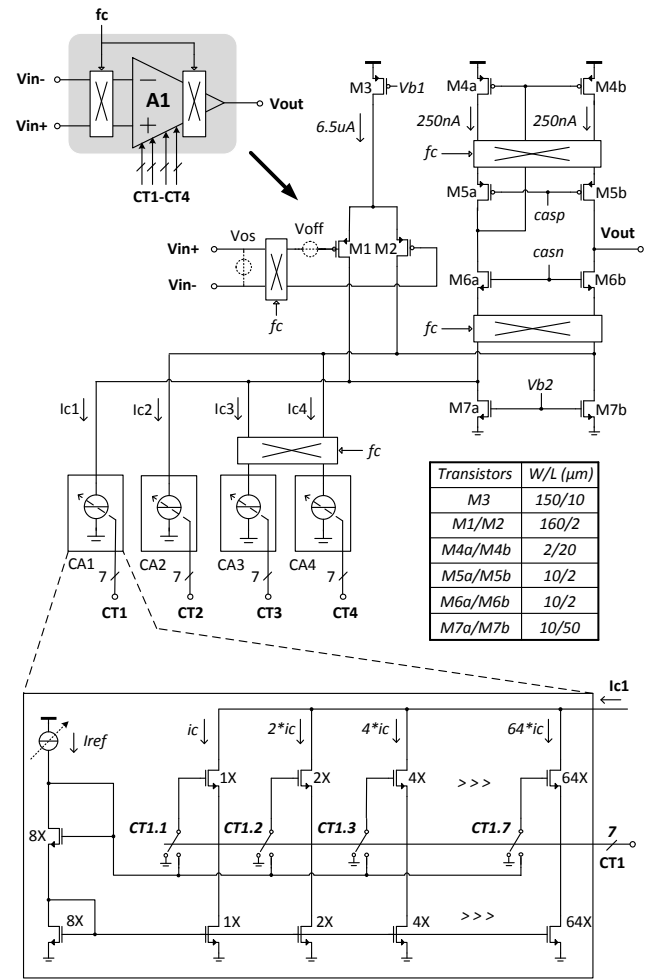


Fig. 4. Chopper amplifier with current DACs.

The auxiliary DACs are used to compensate for the non-idealities of the chopper amplifier. The first pair of current DACs (CA_1 and CA_2) trims the amplifier's offset V_{off} by providing compensation currents (I_{c1} - I_{c2}) to the auxiliary inputs of the core amplifier. Therefore, the output ripple due to the up-modulated V_{off} is reduced. Another pair of current DACs (CA_3 and CA_4) trims the residual offset V_{os} associated with non-idealities of the input chopper by providing modulated compensation currents (I_{c3} - I_{c4}). Therefore, the output residual offset of the amplifier is reduced as well. The detailed operation of the output ripple and residual offset compensation will be discussed in section B. 2).

The current DAC (Fig. 4) consists of an array of cascode current mirrors, whose output current (I_{c1}) is controlled by 7-bit binary inputs ($CT_{1.1}$ - $CT_{1.7}$). This output current is proportional to the reference current source I_{ref} , which can be adjusted by an external resistor. Therefore, the full-scale output current of the first pair of DAC can be flexibly adjusted to compensate for a wide range of input offset voltages. However, due to the finite resolution of the current DACs, there will be some residual offset error, which is given by:

$$V_{off,error} = \frac{I_{ref}}{8g_{m1,2}}, V_{os,error} = \frac{I_{ref2}}{8g_{m1,2}} \quad (5)$$

Where I_{ref} and I_{ref2} are the reference current of CA_1 (CA_2) and CA_3 (CA_4), respectively, $g_{m1,2}$ is the transconductance of the input transistor M_1 and M_2 .

2) Digitally-Assisted Offset Trimming

Two challenges associated with chopper amplifiers are how to reduce their output ripple and residual offset [29] (Fig. 5). The output ripple is due to the amplifier's up-modulated offset voltage V_{off} , and resembles a low-pass filtered square wave. Compared to the μV level biopotential signals, the ripple can be quite large and will, therefore, limit the amplifier's output headroom. As shown in (6), a 5 mV input offset V_{off} of the core amplifier can cause approximately 500 mV output ripple, at the maximum closed-loop gain of 100 ($C_1/C_2=100$). Hence, the amplifier in [29] employs a ripple reduction loop to sense and compensate output ripple. However, it operates continuously and thus increases the amplifier's power consumption.

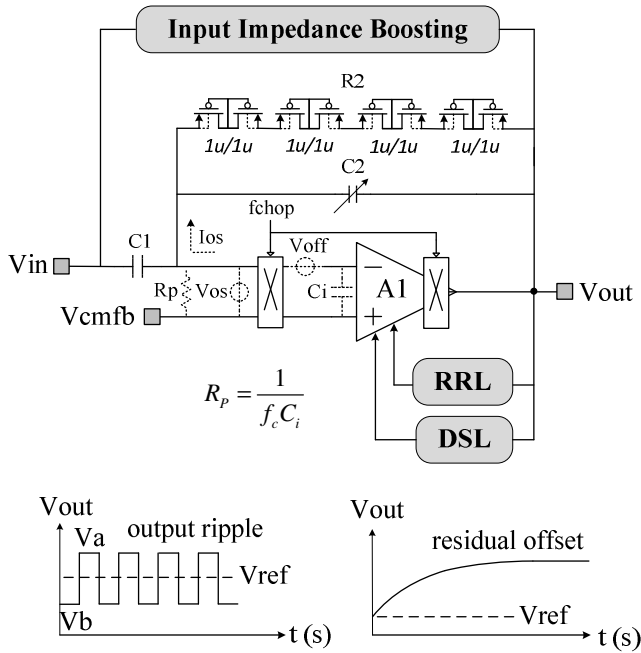


Fig. 5. Chopper-associated output ripple and residual offset.

$$|V_{ripple,pp}| = |V_{off}| \cdot \left(\frac{C_1 + C_2}{C_2} \right) \quad (6)$$

The residual output offset $V_{off,out}$ (Fig. 5) is caused by the spikes of the input chopper [30], which in return are due to the charge injection mismatch of the switches. The spikes are demodulated by the output chopper and the result is a residual output offset. This can be expressed as in (7), where I_{os} is the

offset current that flows through the pseudo-resistor R_2 , C_i is the input capacitance of the amplifier, R_p is the parasitic switched-capacitor resistor formed by input chopper and C_i . The residual offset can be compensated by a DC servo loop with G_m -C filter [21]. However, this requires a large off-chip capacitor ($>10 \mu F$) to realize a sufficiently low cutoff frequency.

$$V_{off,out} = I_{os}R_2 = \frac{V_{os}R_2}{R_p} = f_c C_i R_2 V_{os} \quad (7)$$

In the proposed active electrode, both the ripple and the offset are suppressed by digitally-assisted foreground calibration loops: a ripple reduction loop (RRL) and a DC servo loop (DSL). It should be noted that the biopotential input signal is not present during the calibration.

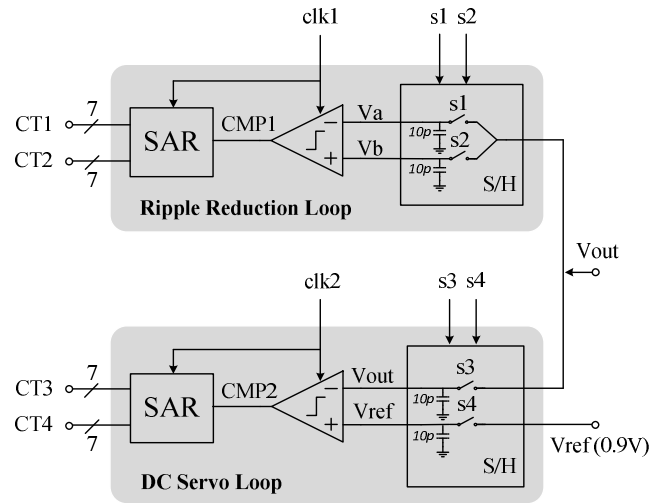


Fig. 6. Block diagrams of the RRL and the DSL.

The calibration starts with the RRL: the peak ripple levels V_a and V_b are synchronously sampled (Fig. 6), and the polarity CMP1 is determined by a comparator. A fully integrated successive approximation algorithm (SAR) generates a pair of 7-bit binary outputs (CT_1 and CT_2) to control a pair of 7-bit current DACs (CA_1 and CA_2 in Fig. 4) respectively. The outputs of the SAR have inverse polarity, so that either a segment from the left DAC (CA_1) or from the right DAC (CA_2) is switched on after each comparison. Therefore, The DACs generate compensation currents (I_{c1} and I_{c2}) to minimize the output ripple in seven clock cycles. The timing of the RRL's operation is illustrated in Fig. 7.

The DSL starts after the RRL and operates in a similar manner (Fig. 6): the output DC voltage V_{out} is sampled and compared to a reference voltage V_{ref} . The comparator output CMP2 is sent to the SAR, whose outputs control another pair of current DACs (CA_3 and CA_4 in Fig. 4). Their outputs are chopper modulated in order to generate a modulated compensation current to reduce any output residual offset. The timing of the DSL's operation is illustrated in Fig. 8.

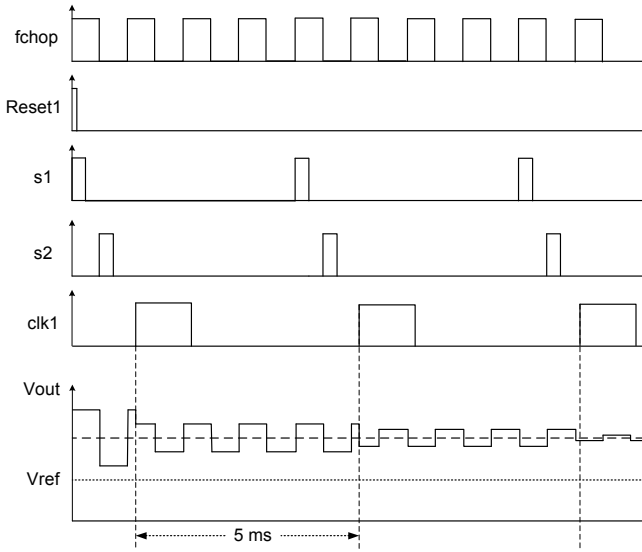


Fig. 7. Timing waveform of the RRL

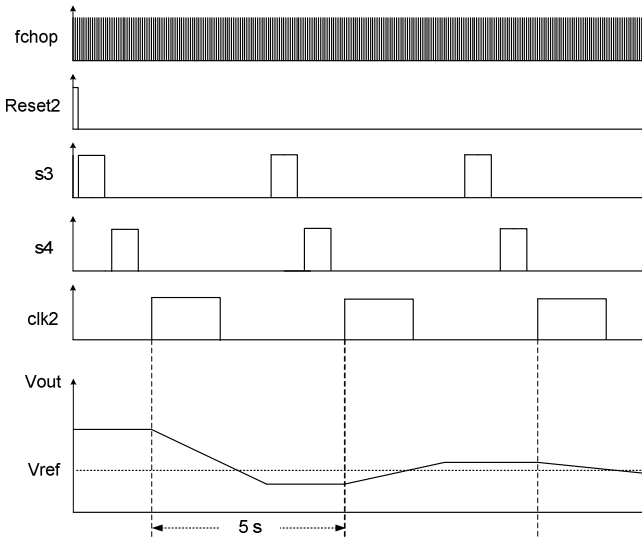


Fig. 8. Timing waveform of the DSL

Once both the RRL and the DSL are finished, the inputs to the current DACs are frozen, the trimming loops are shut-down and normal mode of biopotential signal amplification starts. Both calibration loops can be reset when necessary, in case there is any drift of the ripple and the offset.

The power dissipation of the RRL and the DSL is mainly determined by the DAC currents, and is less than 400nW in total.

3) Input-Impedance Boosting Loop

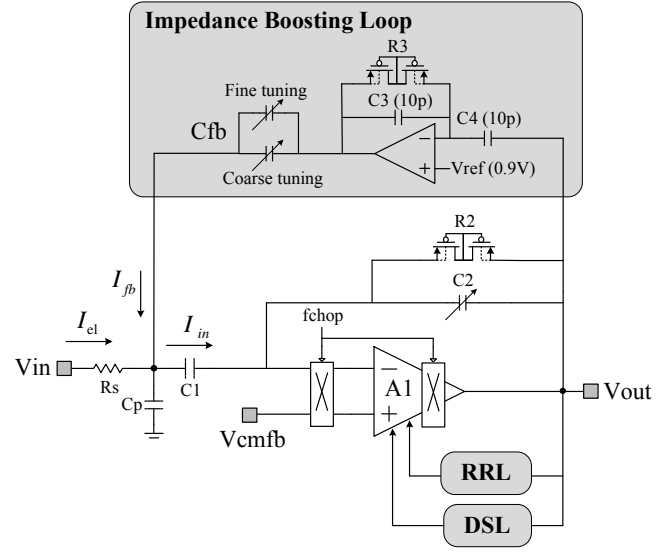


Fig. 9. Input-impedance boosting via partial positive feedback.

Without the input-impedance boosting loop (Fig. 9), the input impedance of the amplifier is dominated by C_1 . This is shown in (8), where C_p is the total parasitic capacitance at the input of the front-end amplifier, e.g. due to bond-pad and wiring parasitic capacitances and R_s is the contact impedance of the skin-electrode interface.

$$Z_m = \frac{1}{s(C_1 + C_p)} + R_s \approx \frac{1}{sC_1} \quad (8)$$

In case C_1 is selected to be 300 pF for low-noise operation (see section B. 4)), the input impedance is limited to approximately 10 M Ω at 50 Hz. This can degrade the CMRR [33] and increase the effect of mains interference on the system. In order to maximize the input impedance of the active electrode front-end, a partial positive feedback loop (Fig. 9) is implemented to boost the amplifier's input impedance [21]. This consists of an AC-coupled inverting amplifier and a capacitor array C_{fb} , which includes C_{fb_coarse} and C_{fb_fine} in parallel. The output AC signal of the core amplifier is inverted and amplified with a gain of C_3/C_4 . Via C_{fb} , this loop continuously supplies current I_{fb} , which is a portion of the total input current I_{in} . Therefore, the current drawn from the recording electrode, I_{el} , is reduced.

The input impedance of the active electrode, after employing the impedance loop, can be expressed as shown in (9). Compared to (8), the equivalent input impedance has been increased by a factor of β , as shown in (10).

$$Z_{in} = \frac{V_{in}}{I_{el}} = \frac{1}{s(C_1 + C_p) - sC_{fb} \left[\frac{s^2 C_1 C_4 R_2 R_3}{(sC_2 R_2 + 1)(sC_3 R_3 + 1)} - 1 \right]} \quad (9)$$

$$\beta = \frac{Z'_{in}}{Z_{in}} = \frac{C_1 + C_p}{C_1 + C_p - C_{fb} \left(\frac{C_1 C_3}{C_2 C_4} - 1 \right)} \approx \frac{C_1 + C_p}{C_1 + C_p - A_{V,IMP} C_{fb}} \quad (10)$$

Where β is the effective impedance boosting factor, Z_{in} is the input impedance without impedance boosting, and Z'_{in} is the input impedance with impedance boosting. Ideally, the input impedance of the amplifier can be boosted to infinitely ($\beta \rightarrow \infty$ and $I_{el} = 0$).

However, this is the threshold condition for stability. Making C_{fb} too large will result in $\beta < 0$, which translates into negative input impedance and an unstable feedback loop, since a portion of the feedback current I_{fb} then flows out into the electrode ($I_{el} < 0$). Therefore, the maximum value of C_{fb} must be limited as in (11) to maintain $\beta > 0$:

$$C_{fb,max} = \frac{C_1 + C_p}{A_V} \quad (11)$$

An additional attention point associated with (10) and (11), is the variation of C_1 and parasitic capacitances C_p . Both can reduce the effective input impedance boosting factor β , and may lead to potential instability ($\beta < 0$). Therefore, C_{fb} is implemented as the combination of a coarse and fine capacitor array, in order to be able to trim the amount of positive feedback to compensate the affect of these process variation and parasitic capacitance. At variable gain settings, the coarse array $C_{fb,coarse}$ is switched in tandem with the value of C_2 . The fine array $C_{fb,fine}$ can then be adjusted to further compensate for the current that flows into C_1 and C_p , thus ensuring that β is high enough to guarantee stability. The selected $C_{fb,fine}$ array (25 pF) can compensate 20% variation of C_1 (at lowest gain $A_V=3$), plus a large C_p up to 15 pF.

4) Noise Analysis of the Front-End Active Electrode

Using the equivalent circuit in Fig. 10, the total input referred noise PSD of the front-end active electrode (FEAE) can be calculated as (12).

$$\begin{aligned} \overline{V_{in,FEAE}^2} &= \left(\overline{V_{in,OTA1}^2} + \overline{V_{in,cmfb}^2} \right) \cdot \left(1 + \frac{C_2}{C_1} + \frac{2\pi f_c C_i}{s C_1} \right)^2 \\ &+ \overline{V_{n,R2}^2} \cdot \left(\frac{1}{s C_1 R_2} \right)^2 + \left(\overline{V_{in,OTA2}^2} + \overline{V_{in,ref}^2} \right) \cdot (2s R_s C_{fb})^2 \\ &+ \left(\overline{V_{in,RRL}^2} + \overline{V_{in,DSL}^2} \right) \cdot \left(\frac{g_{m,DAC}}{g_{m1}} \right)^2 \end{aligned} \quad (12)$$

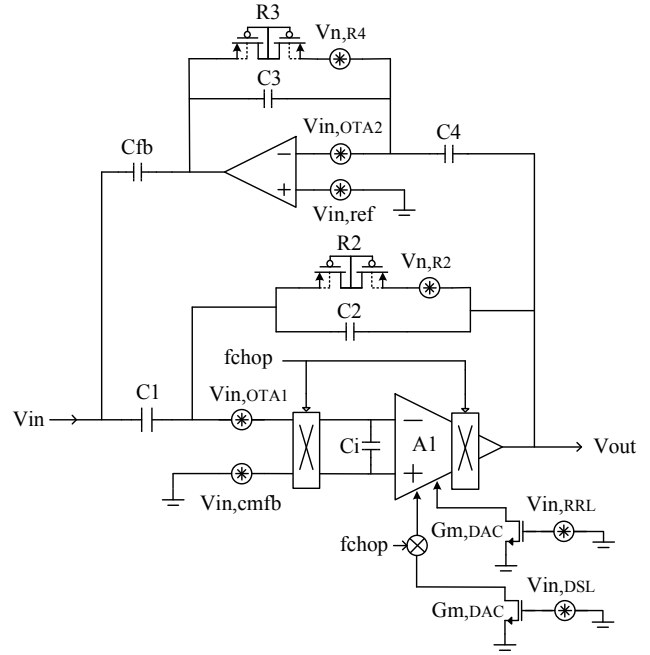


Fig. 10. Equivalent circuit for calculating the input referred noise of the front-end active electrode.

Where $\overline{V_{in,FEAE}^2}$ is the total input referred noise of the front-end active electrode, $\overline{V_{in,OTA1}^2}$ is the input referred noise of the core chopper amplifier A_1 , $\overline{V_{in,cmfb}^2}$ is the noise from the back-end CMFB amplifier, $\overline{V_{n,R2}^2}$ is the noise contribution of the pseudo-resistor R_2 , $\overline{V_{in,ref}^2}$ is the noise of the reference voltage, which bias the inverting amplifier in the impedance boosting loop, $\overline{V_{in,RRL}^2}$ and $\overline{V_{in,DSL}^2}$ are the noise contribution from the RRL and the DSL, $g_{m,DAC}$ is the effective transconductance of the current DAC, g_{m1} is the transconductance of the input pair of the core amplifier A_1 , respectively.

The noise contribution of the impedance boosting loop ($\overline{V_{in,OTA2}^2}$ and $\overline{V_{in,ref}^2}$) is negligible as long as $1/sC_{fb}$ is much larger than R_s . The noise generated from pseudo-resistor R_2 is also very small as $sC_1 R_2$ is much larger than 1. The noise from the RRL and the DSL is not dominant either, because g_{m1} of the core amplifier input pair is much larger than $g_{m,DAC}$. The noise from the CMFB input is common-mode noise in a multi-channel active electrode system. Hence, the total input referred noise of single active electrode can be approximated as:

$$\overline{V_{in,FEAE}^2} = \overline{V_{in,OTA1}^2} \cdot \left(1 + \frac{C_2}{C_1} + \frac{2\pi f_c C_i}{s C_1} \right)^2 \quad (13)$$

This is approximately equal to the thermal noise PSD of the core chopper amplifier, multiplied by a noise shaping factor, which is due to the parasitic switched-capacitor resistor and exhibits a $1/f^2$ frequency characteristic [21].

Several design considerations should be taken into account to minimize the noise shaping factor in (13). A large coupling capacitor C_1 should be used as long as the input impedance still meets the design specifications. The chopping frequency f_c should be selected very close to the $1/f$ corner of the core amplifier, so that a minimal f_c of 500 Hz is selected without compromising the noise floor of the chopper amplifier significantly. Moreover, the input parasitic capacitor C_i (Fig. 10) can be reduced by careful layout.

C. Back-end CMFB amplifier

The back-end CMFB circuit can improve the CMRR of the active electrode system. Fig. 11 shows the equivalent circuit of a simplified two-active electrode system and demonstrates the CMRR improvement. Without the back-end CMFB (Fig. 11(a)), both CM inputs are referred to ground. Therefore, the differential output V_{out} is proportional to the gain mismatch (ΔA_V) of the active electrodes, and the CMRR without the back-end CMFB is shown in (14).

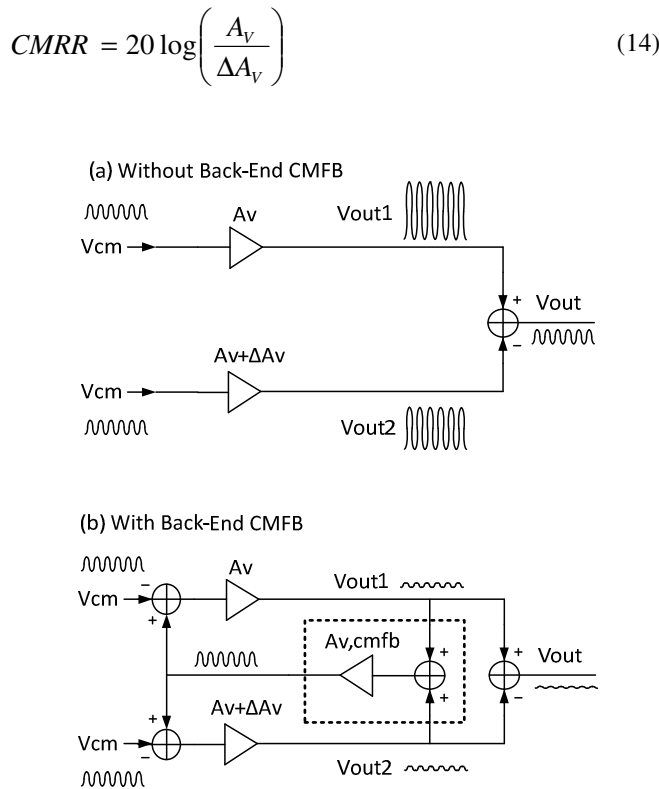


Fig. 11. The equivalent circuit of the proposed active electrode system, (a) without and (b) with back-end CMFB.

With the back-end CMFB (Fig. 11(b)), however, the positive inputs of the core amplifiers are connected to the output of the back-end CMFB. Therefore, the CM inputs are referred to the

output voltage of the back-end summing amplifier, which is approximately equal to the CM input of all channels. Thanks to the back-end CMFB, which reduces the CM gain, the residual CM outputs V_{out1} and V_{out2} , as well as the differential output V_{out} . The improved CMRR' by using back-end CMFB is shown in (15), where it has been improved approximately by a factor of $20 \cdot \log(A_V)$ compared to (14), where A_V is the close-loop voltage gain of the active electrode, and $A_{V,CMFB}$ is the CM gain of the capacitive summing amplifier.

$$CMRR' = CMRR \cdot 20 \log \left(\frac{2A_V}{2 + \frac{1}{A_{V,CMFB}}} + 1 \right) \quad (15)$$

$$\approx CMRR \cdot 20 \log(A_V)$$

The CMRR improvement is mainly limited by the voltage gain A_V of the front-end amplifier and the voltage gain $A_{V,CMFB}$ of the summing amplifier, as shown in (15). Therefore, in order to achieve a maximum CMRR improvement, both high A_V of 100 and $A_{V,CMFB}$ of 16 are implemented.

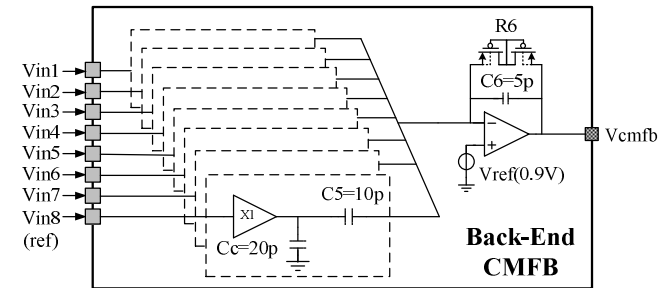


Fig. 12. Block diagram of back-end CMFB circuit.

The back-end CMFB circuit (Fig. 12) consists of a capacitive summing amplifier to provide common-mode (CM) gain $A_{V,CMFB} = 8 \cdot (C_5/C_6)$, and eight unit-gain G_m -C low-pass filters to reject high-frequency interference. This summing amplifier only feeds the average CM voltage of all 8 active electrodes back to each of the active electrodes, while rejecting any differential-mode (DM) signals.

Any two active electrodes can be used to form a bipolar channel (Fig. 3). Although the common-mode signal (V_{cmfb}) still present at output of each electrode, actual EEG signals are always measured differentially between electrodes. As a result, the common-mode signal is removed as shown below:

$$\begin{aligned} V_{out1} - V_{out8} &= (V_{in1} - V_{cmfb})A_V - (V_{in8} - V_{cmfb})A_V \\ &= (V_{in1} - V_{in8})A_V \end{aligned} \quad (16)$$

Therefore, the back-end circuit can provide a continuous-time CMFB signal without disturbing the differential EEG signals recording between any two active

electrodes.

The capacitive summing amplifier blocks the residual output offsets of the active electrodes, thus avoids amplifier saturation. Via pseudo-resistor R_6 , the reference voltage V_{ref} provides the same bias voltage to all active electrodes.

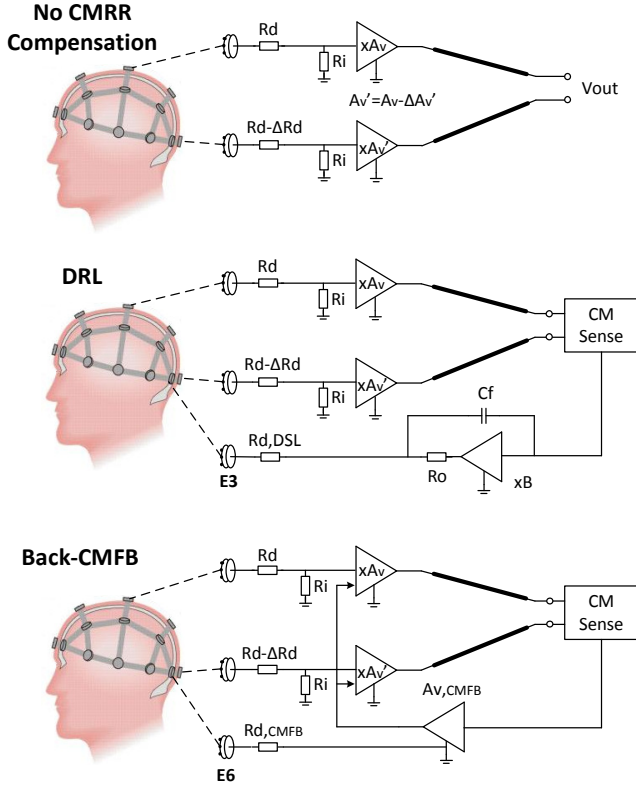


Fig. 13. Block diagrams of the DRL and the back-end CMFB

Without any CMRR compensation (Fig. 13), the CMRR of an active electrode pair is limited by both contact impedance mismatch (ΔR_d) and amplifier component mismatch (ΔA_v), this is shown in (17).

$$CMRR = 20 \log \left(\frac{A_v}{\Delta A_v + \frac{A_v \Delta R_d}{R_d + R_i}} \right) \quad (17)$$

Compared to the well known Driven-Right-Leg (DRL) circuit [31] (Fig. 13), the proposed back-end CMFB circuit feeds the CM signal back to the amplifier, instead of the patient. Therefore, the back-end CMFB circuit improves the CMRR limited by amplifier component mismatch (ΔA_v). Even if this is very good, the maximum CMRR, that the back-end CMFB circuit can achieve, will ultimately be limited by contact impedance mismatch (ΔR_d), as shown in (18).

$$CMRR_{CMFB_max} = 20 \log \left(\frac{R_d + R_i}{\Delta R_d} \right) \quad (18)$$

On the other hand, the DRL circuit feeds the CM signal back to the patient through an additional DRL electrode (E3), which improves CMRR due to both components mismatch (ΔA_v) and contact impedance mismatch (ΔR_d). As a result, the maximum CMRR with a DRL circuit is theoretically infinite.

However, due to the variability of the electrode impedances $R_{d,DSL}$ ($k\Omega$ - $M\Omega$) and the stray capacitance, the DRL circuit must be carefully designed to ensure it is always stable [31], which requires large feedback capacitor C_f (10nF) for stability compensation [32]. This will be more difficult with dry electrodes, since the electrode impedance is even more variable. In contrast, the variation of electrode impedance ($R_{d,CMFB}$) does not affect the stability of the back-end CMFB circuit, as the third electrode (E6) biases the patient to the circuit ground.

III. MEASUREMENT RESULTS AND DISCUSSIONS

A. Measurement of Performance

The chip has been implemented in a $0.18 \mu m$ standard CMOS process and occupies less than 6.5 mm^2 (Fig. 14). Each fabricated die contains one front-end active electrode and one back-end circuit. Therefore, 9 chips are sufficient to realize an 8-channel EEG monitoring system with a single separate chip operating as back-end CMFB. The 8-channel system, including both front-end and back-end circuits, consumes in total $160 \mu W$ from 1.8V, additional power is required for clock generation.

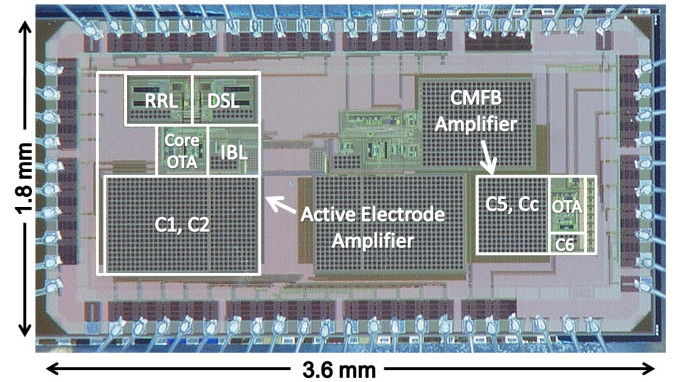


Fig. 14. Chip photograph.

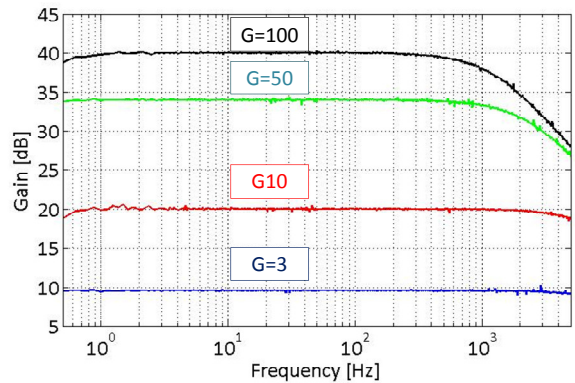


Fig. 15. Measured various gain of active electrode.

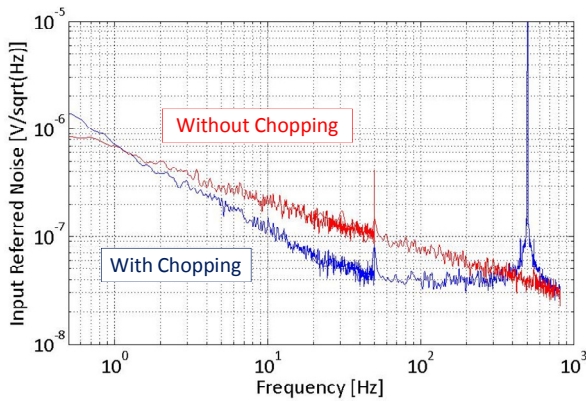


Fig. 16. Measured input referred noise of one active electrode.

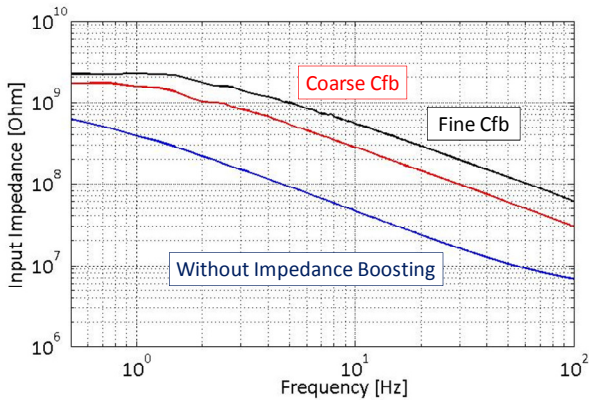


Fig. 17. Measured input impedance of active electrode.

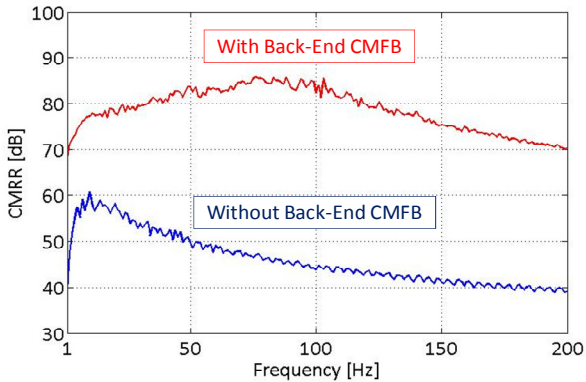


Fig. 18. Measured CMRR between electrode pair.

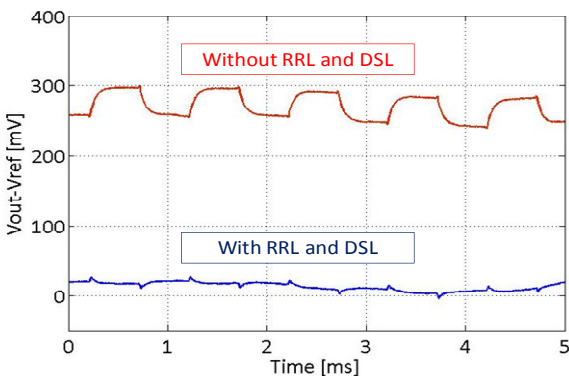


Fig. 19. Measured output ripple and residual offset.

Fig. 15 shows the measured voltage gain from the front-end active electrode, demonstrating the programmable gain from 3 to 100. Fig. 16 shows the input referred noise with and without chopping. Chopping at 500 Hz leads to a total input referred noise voltage of $0.8 \mu\text{Vrms}$ (0.5-100 Hz) compared to $1.5 \mu\text{Vrms}$ without chopping. Fig. 17 shows the input impedance without impedance boosting: $400 \text{ M}\Omega$ at 1 Hz, and the increased input impedance achieved by enabling the impedance boosting loop: $2 \text{ G}\Omega$ at 1 Hz. Fig. 18 shows the CMRR of a pair of active electrodes, which are configured with a voltage gain of 100. An 82 dB CMRR has been measured around 50 Hz by employing the proposed back-end CMFB circuit, which improves the CMRR, by more than 30 dB. Fig. 19 shows the output waveforms before and after ripple and residual offset trimming, when the active electrode is configured with a maximum voltage gain of 100. The output ripple has been reduced to less than 2 mV compared to the initial 40 mV. The DC servo-loop also successfully reduces the output offset from 280 mV to 20 mV.

TABLE I

COMPARISON TABLE OF THE PROPOSED ACTIVE ELECTRODE WITH THE STATE-OF-THE-ART ASICs FOR BIOPOTENTIAL SIGNALS ACQUISITION

Parameters	[19]	[23]	[17]	[22]	This work
Supply	1.8V	3V	1V	1V	1.8V
Voltage gain	100	10	190-1000	100	3-100
Input impedance	$>7.5 \text{ M}\Omega$	$>100 \text{ M}\Omega$	--	$>700 \text{ M}\Omega$	$>2 \text{ G}\Omega$
Input referred noise	$0.95 \mu\text{Vrms}$ (0.05-100 Hz)	$0.6 \mu\text{Vrms}$ (0.5-100 Hz)	$2.5 \mu\text{Vrms}$ (0.05-460 Hz)	$1.3 \mu\text{Vrms}$ (0.5-100Hz)	$0.8 \mu\text{Vrms}$ (0.5-100 Hz)
Electrode offset rejection	50mV	50mV	Rail-to-rail	Rail-to-rail	Rail-to-rail
CMRR	100dB	120dB	71dB	60dB	82dB
Current	$1.1 \mu\text{A}$	$11.1 \mu\text{A}$	337nA	$3.5 \mu\text{A}$	$11 \mu\text{A}$
NEF	4.6	9.2	3.26	--	12.3
Dry electrode applications	No	No	No	No	Yes

Table I summarizes the circuit performance and compares it with state-of-the-art implementations. Compared to these, the proposed amplifier achieves the highest input impedance, comparable input referred noise, and a good balance between electrode offset rejection and CMRR. Furthermore, the other implementations are implemented with differential amplifiers, while it is preferable to use a single-ended amplifier as an active electrode. The problem of achieving high CMRR between single-ended amplifiers is their gain mismatch. This problem is essentially solved by the use of a back-end CMFB circuit. These features make the proposed system well suitable for gel-free active electrode recording.

B. Suppression of Cable Motion Artifacts and Interference

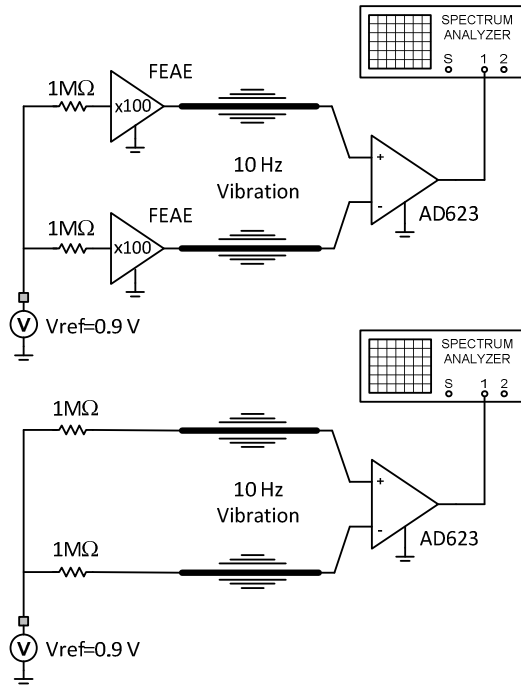


Fig. 20. Cable motion artifacts reduction test by introducing cable vibration.

This section discusses the benefits of active electrode readout compared to passive electrode readout, in terms of cable motion artifacts and interference. Fig. 20 shows the test setup to compare active electrode readout and passive electrode readout in terms of their robustness to cable motion artifacts. Two 1 MΩ resistors are placed at input to mimic the contact impedance of a gel-free electrode. A low-noise, high input-impedance and high CMRR instrumentation amplifier AD623 [34], configured with a voltage gain of 100, is used as a conventional biopotential amplifier for comparison purposes. The cables connected to AD623 are attached to a vibration device that vibrates constantly at 10 Hz. Fig. 21 shows the measured input-referred spectrum. A significant reduction of 10 Hz cable motion artifacts is observed for the active electrode readout circuit due to its relatively low output impedance.

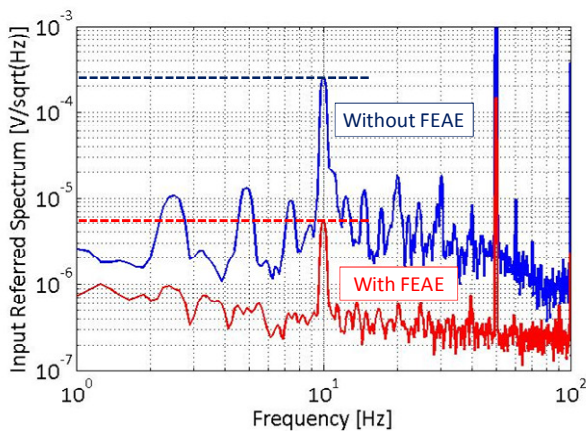


Fig. 21. The comparison of measured cable motion artifacts.

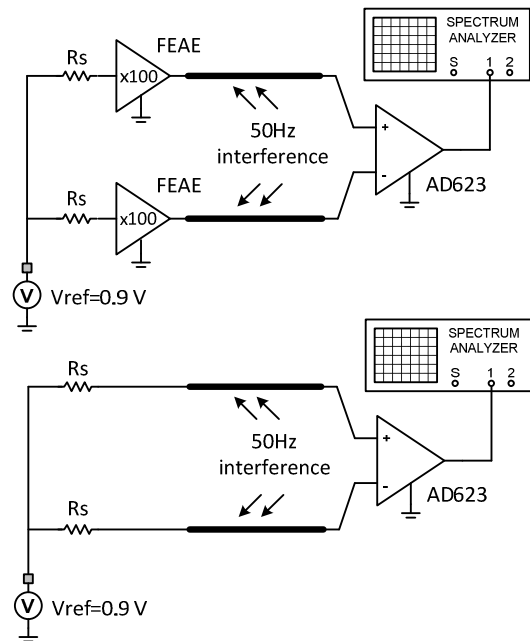


Fig. 22. Interference reduction test by introducing 50 Hz interference source.

Fig. 22 shows the test setup comparing the input-referred 50 Hz interference picked up via the cable, again with and without active electrode. The cables are placed on top of two power plugs, which generate almost constant 50 Hz power line interference. A pair of variable resistors R_S are placed in series with the voltage source to mimic the skin-electrode impedance. Fig. 23 shows the measured input-referred 50 Hz interference of the two systems versus source impedance R_S . The input-referred 50 Hz component is low and almost constant for the active electrode readout circuit, while it increases linearly until $R_S = 1$ MΩ for the passive electrode readout circuit. The advantage of the active electrode readout circuit is more appreciated when $R_S > 10$ kΩ, which is the typical range of the contact impedance of a gel-free electrode [6].

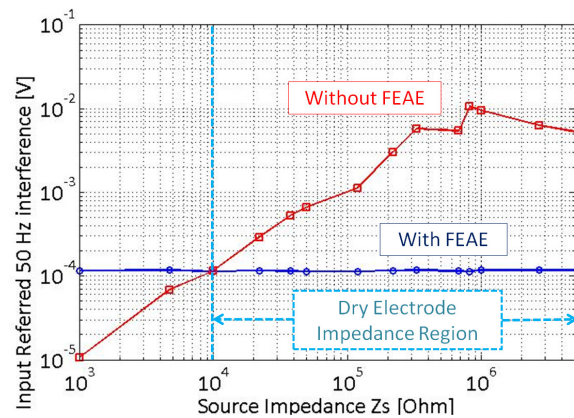


Fig. 23. The comparison of measured 50 Hz interference.

C. EEG Measurements

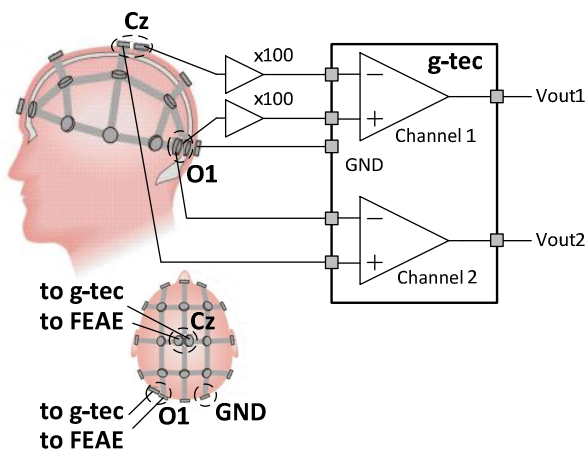


Fig. 24. The EEG measurement setup.

Fig. 24 shows the test setup for EEG measurement. For simplicity, EEG signals are measured between two pairs of electrodes, which are placed in positions of O1 and Cz. A first pair is connected to two active electrode test boards through short wires. The outputs of these boards are connected to the computer through a commercial biopotential recording system (g.USBamp from g-tec) [35]. For comparison, another pair of electrodes is placed very close to the first pair. The outputs of these electrodes are directly connected to the g.USBamp system. In this way, EEG signals can be measured and compared synchronously between the active electrode system and an existing commercial passive electrode system.

In the first measurement, both systems use wet electrodes. Fig. 25 shows the spectrogram of the measured EEG signal during eyes open and eyes closed. Alpha waves at 10 Hz during the eyes closed period are clearly visible. Moreover, in Fig. 26, the spectrum correlation coefficient (ρ) between wet active electrode system and wet passive electrode system is higher than 0.99, indicating a very comparable performance between these two types of wet electrode systems.

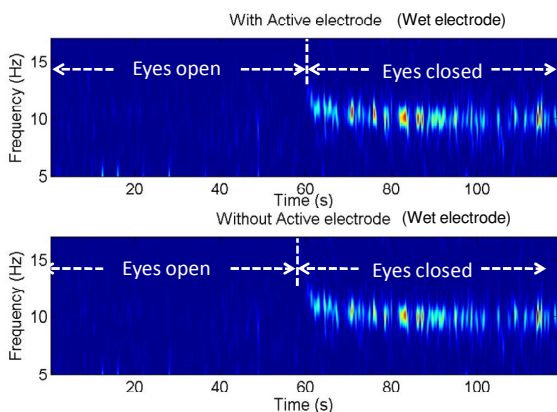


Fig. 25. EEG spectrogram with active electrodes (upper trace, wet electrodes) and without active electrodes (bottom trace, wet electrodes)

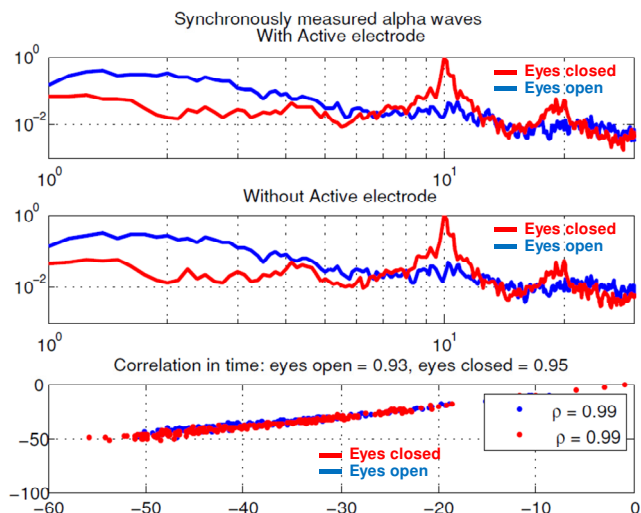


Fig. 26. EEG normalized spectrum with and without active electrode (both with wet electrode). Eyes open (blue curve) and eyes closed (red curve).

In the second measurement, wet electrodes are replaced with dry electrodes, which are embedded on an IMEC-developed EEG headset [39]. The g.USBamp system still uses wet electrodes in the same position. Fig. 27 shows the spectrogram of the measured EEG signal during eyes open and eyes closed. Alpha waves at 10 Hz during the eyes closed period are still clearly visible for the both systems. Moreover, in Fig. 28, the spectrum correlation coefficient (ρ) between the dry active electrode system and the wet passive electrode system is higher than 0.93, which shows that the active electrode system, even with gel-free contact, can still achieve comparable performance to the g.USBamp wet electrode system. This correlation coefficient is also high in comparison to other work on dry electrode sensing, such as [36]: $\rho > 0.9$, [37]: $\rho = 0.8 - 0.96$ and [38]: $\rho = 0.83$.

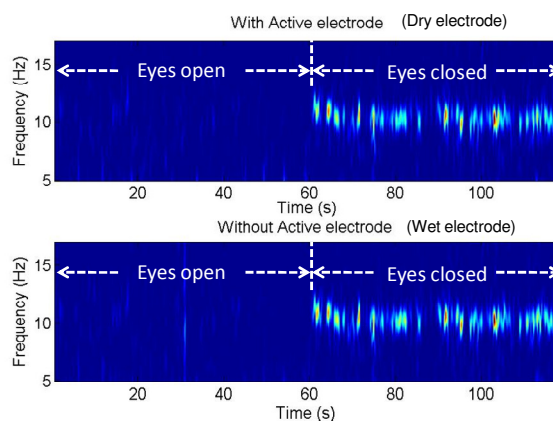


Fig. 27. EEG spectrogram with active electrodes (upper trace, dry electrode headset) and without active electrodes (bottom trace, wet electrode)

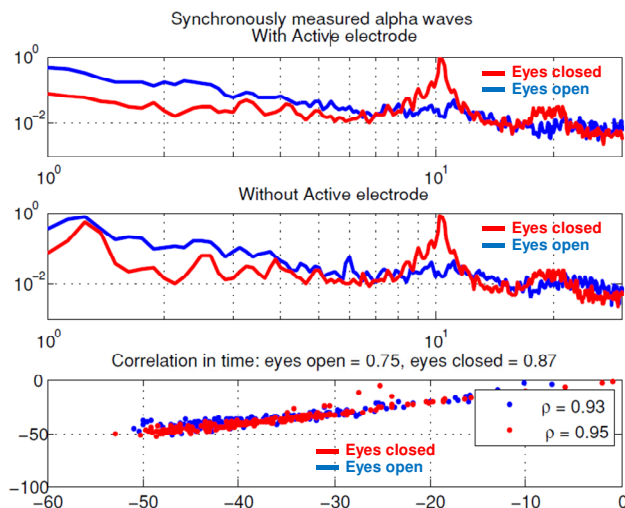


Fig. 28. EEG normalized spectrum with active electrode (dry electrode headset) and without active electrode (wet electrode). Eyes open (blue curve) and eyes closed (red curve).

IV. CONCLUSION

The development of portable ambulatory biopotential monitoring systems for miniaturized and personalized non-clinical applications requires both user-friendly gel-free electrodes and low-power high-performance readout circuits. However, state-of-the-art circuit implementations are not well suited for the low-power gel-free EEG recordings.

Therefore, this paper, for the first time, has presented a low-power active electrode ASIC system for EEG monitoring applications using gel-free electrodes.

The proposed system includes eight front-end amplifiers as active electrodes and one extra back-end CMFB amplifier for CMRR improvement. The AC-coupled chopper amplifier, combined with input-impedance boosting, ripple and offset trimming, and CMRR enhancement, achieves state-of-the-art performance of $0.8 \mu\text{V}_{\text{rms}}$ (0.5-100 Hz) input referred noise, 2 G Ω input impedance, 40mV residual output offset, 2mV output ripple, as well as 82dB CMRR between each electrode pair.

The benefits of the active electrode readout over the traditional passive electrode readout, in terms of reduced cable motion artifacts and mains interference, are also demonstrated.

Biological EEG measurement shows that the proposed active electrode system can measure typical EEG features, such as alpha waves, with both wet and dry electrodes. Moreover, in comparison to an existing commercial wet electrode system, both wet and dry active electrode systems show very highly correlated EEG recording results.

ACKNOWLEDGMENT

The authors would like to thank Prof. J. H. Huijsing, Q. Fan and S. Patki for valuable discussion.

REFERENCES

[1] E. Waterhouse, "New horizons in ambulatory electroencephalography," *Engineering in Medicine and Biology Magazine, IEEE*, vol. 22, no. 3, pp. 74-80, 2003.

[2] S. Park and S. Jayraman, "Enhancing the quality of life through wearable technology," *Engineering in Medicine and Biology Magazine, IEEE*, vol. 22, no. 3, pp. 41-48, May/June 2003.

[3] A. Casson, D. Yates, S. Smith, J. Duncan, E. Rodriguez-Villegas, "Wearable Electroencephalography," *Engineering in Medicine and Biology Magazine, IEEE*, vol. 29, no. 3, pp. 44-56, May-June 2010.

[4] Lin C-T, Ko L-W, Chang M-H, Duann J-R, Chen J-Y, Su T-P, Jung T-P, "Review of Wireless and Wearable Electroencephalogram Systems and Brain-Computer Interfaces - A Mini-Review," *Gerontology*, 56: pp 112-119, 2010.

[5] G. E. Bergey, et al., "Electrocardiogram recording with pasteless electrodes," *IEEE Trans. Biomed. Eng.*, vol. BME-18, pp. 206-211, May 1971.

[6] Y. M. Chi, Tzyy-Ping Jung; G. Cauwenberghs, "Dry-Contact and Noncontact Biopotential Electrodes: Methodological Review," *IEEE Reviews in Biomedical Engineering*, pp.106-119, 2010.

[7] S. Nishimura, Y. Tomita, T. Horiuchi., "Clinical application of an active electrode using an operational amplifier," *IEEE Trans on Biomed Eng.* vol. 39, pp. 1096 - 1099, 1992.

[8] F. Z. Padmadinata, J. J. Veerhoek, G. J. A. van Dijk and J. H. Huijsing, "Microelectronic skin electrode," *Sensors and Actuators B: Chemical* Volume 1, Issues 1-6, pp 491-494, 1990.

[9] M. Fernandez and R. Pallas-Areny., "A simple active electrode for power line interference reduction in high resolution biopotential measurements," *IEEE Engineering in Medicine and Biology Society*, vol.1, pp.97-98. 1997.

[10] T. Degen, S. Torrent, H. Jackel., "Low-Noise Two-Wired Buffer Electrodes for Bioelectric Amplifiers," *IEEE Trans on Biomed Eng.* vol. 54, pp. 1328 - 1332, 2007.

[11] A. C. Metting van Rijn, A. P. Kuiper, T. E. Dankers, C. A. Grimbergen, "Low cost active electrode improves the resolution in biopotential recordings." In Proceedings of the 18th Ann Int Conf IEEE Eng Med Bio, pp 101-102, 1996.

[12] A. C. Metting van Rijn, A. Peper, and C. A. Grimbergen, "High-quality recording of bioelectric events. Part I: Interference reduction, theory and practice," *Med. Bio. Eng. Comput.* vol. 28, pp. 389-397, Sept, 1990.

[13] Y.M. Chi, G. Cauwenberghs, "Wireless Non-contact EEG/ECG Electrodes for Body Sensor Networks," in *International Conf on Body Sensor Networks (BSN)*, pp. 297-301, 2010.

[14] R. Matthews, N. McDonald et al., "The invisible electrode-zero prep time, ultra low capacitive sensing". Proceedings of the 11th International Conference on Human Computer Interaction (2005).

[15] R. R. Harrison and C. Charles, "A Low-Power Low-Noise CMOS Amplifier for Neural Recording Applications," *IEEE J. Solid-State Circuits*, pp. 958-965, June 2003.

[16] W. Wattanapanitch, M. Fee, and R. Sarpeshkar, "An energy-efficient micropower neural recording amplifier," *IEEE Trans. Biomedical Circuits Syst.*, vol. 1, pp. 136-147, 2007.

[17] X. Zou, W. Liew, L. Yao, L. Yong, "A 1-V 450-nW Fully Integrated Programmable Biomedical Sensor Interface Chip," *IEEE J. Solid-State Circuits*, pp. 1067-1077, April 2009.

[18] H. Wu, Y. Xu., "A 1V 2.3 μW Biomedical Signal Acquisition IC," *ISSCC Dig. Tech. Papers*, pp. 119-128, 2006.

[19] T. Denison, K. Consoer, A. Kelly et al., "A 2.2 μW 94nV/ $\sqrt{\text{Hz}}$ Chopper-Stabilized Instrumentation Amplifier for EEG Detection in Chronic Implants," *ISSCC Dig. Tech. Papers*, pp. 162-594, 2007.

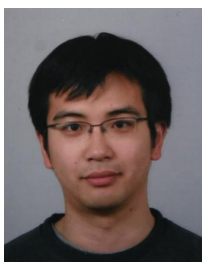
[20] A.-T. Avestruz, W. Santa, D. Carlson, R. Jensen, S. Stanslaski, A. Helfenstine, T. Denison., "A 5 μW /Channel Spectral Analysis IC for Chronic Bidirectional Brain-Machine Interfaces" *IEEE J. Solid-State Circuits*, pp. 3006-3024, Dec 2008.

[21] Q. Fan, F. Sebastiano, H. Huijsing, K. A. A. Makinwa., "A 1.8 μW 60 nV/ $\sqrt{\text{Hz}}$ Capacitively-Coupled Chopper Instrumentation Amplifier in 65nm CMOS for Wireless Sensor Nodes," *IEEE J. Solid-State Circuits*, pp. 1534-1543, July 2011.

[22] N. Verma, A. Shoeb, A. J. Bohorquez et al., "A Micro-Power EEG Acquisition SoC With Integrated Feature Extraction Processor for a Chronic Seizure Detection System," *IEEE J. Solid-State Circuits*, pp. 804-816, April 2010.

[23] R. F. Yazicioglu, P. Merken, R. Puers et al., "A 60 μW 60 nV/ $\sqrt{\text{Hz}}$ Readout Front-End for Portable Biopotential Acquisition Systems," *IEEE J. Solid-State Circuits*, pp. 1100-1110, May 2007.

- [24] M. R. Nuwer *et al.*, "IFCN standards for digital recording of clinical EEG," *Electroencephalogr. Clin. Neurophysiol.*, vol. 106, no. 3, pp. 259–261, Mar. 1998.
- [25] J. Xu, R.F. Yazicioglu, P. Harpe, K. A. A. Makinwa, C. Van Hoof, "A 160 μ W 8-channel active electrode system for EEG monitoring," *ISSCC Dig. Tech. Papers*, pp. 300–302, 2011.
- [26] R. H. Olsson, III, M. N. Gulari, and K. D. Wise, "Silicon neural recording arrays with on-chip electronics for in-vivo data acquisition," in *Proc. IEEE-EMBS Special Topic Conf. Microtechnol. Medicine Biol.*, pp. 237–240, 2002.
- [27] M. Sanduleanu *et al.*, "A low noise, low residual offset, chopped amplifier for mixed level applications," in *Proc. IEEE Int. Conf. Electron., Circuits Syst.*, vol. 2, pp. 333–336, 1998.
- [28] W. Sansen, *Analog Design Essentials*. New York: Springer, 2006.
- [29] R. Wu, K.A.A. Makinwa, J. H. Huijsing, "A Chopper Current-Feedback Instrumentation Amplifier With a 1 mHz 1/f Noise Corner and an AC-Coupled Ripple Reduction Loop," *IEEE J. Solid-State Circuits*, pp. 3232–3243, Dec 2009.
- [30] C. C. Enz and G. C. Temes, "Circuit techniques for reducing the effects of op-amp imperfections: Autozeroing, correlated double sampling, and chopper stabilization," *Proc. IEEE*, vol. 84, pp. 1584–1614, 1996.
- [31] Bruce B. Winter, John G. Webster, "Driven-Right-Leg Circuit Design", *IEEE Trans on Biomedical Engineering*, Vol. BME-30, No. 1, pp.62–66, Jan. 1983.
- [32] T. Degen and H. Jackel, "Enhancing interference rejection of preamplified electrodes by automated gain adaption," *IEEE Trans. Biomed. Eng.*, vol. 51, no. 11, pp. 2031–2039, Nov. 2004.
- [33] T. Jochum, T. Denison, P. Wolf., "Integrated circuit amplifiers for multi-electrode intracortical recording," *J. Neural Eng.*, Vol.6, No. 1, 2009.
- [34] AD623[Online] available at http://www.analog.com/static/imported-files/data_sheets/AD623.pdf
- [35] g.USBamp [Online] available at <http://www.gtec.at/Products/Hardware-and-Accessories/g.USBamp-Specs-Features>
- [36] R. Matthews, P. J. Turner, N. J. McDonald, K. Ermolaev, T. Mc Manus, R. A. Shelby, M. Steindorf, "Real time workload classification from an ambulatory wireless EEG system using hybrid EEG electrodes," *30th Annual International Conference of the IEEE Engineering in Medicine and Biology Society*, pp.5871–5875, Aug 20–25, 2008.
- [37] J. R. Estep, J. C. Christensen, J. W. Monnin, I. M. Davis, G. F. Wilson "Validation of a Dry Electrode System for EEG," *Human Factors and Ergonomics Society Annual Meeting Proceedings*, Volume 53, Number 18, pp. 1171–1175(5), 2009.
- [38] G. Gargiulo, P. Bifulco, R. A. Calvo, M. Cesarelli, C. Jin, A. van Schaik, "A mobile EEG system with dry electrodes," *IEEE Biomedical Circuits and Systems Conference*, 2008, pp.273–276, Nov 2008.
- [39] L. Brown, J. van de Molengraft, R. F. Yazicioglu, T. Torfs, J. Penders, C. Van Hoof., "A low-power, wireless, 8-channel EEG monitoring headset," *IEEE EMBC*, pp.4197–4200, 2010.



Jiawei Xu received the B.Sc. degree in Electronics Eng. from Beijing University of Technology, China, in 2004 and the M.Sc. degree in Microelectronics from Delft University of Technology, The Netherlands, in 2006. From 2006, he joined imec/Holst Centre in Eindhoven, The Netherlands, where he worked on low-power readout circuitry for nanowire-based gas sensor. From 2010, he started working on ultra-low-power biopotential interface circuitry towards the Ph.D. in cooperation with Delft University of Technology. His research interests

include ultra-low-power and low-noise amplifiers for biomedical applications.



Refet Firat Yazicioglu (M'11) has received the Ph.D. degree in Electronics Eng. from Katholieke Universiteit Leuven, Belgium, in 2008. He is currently employed at IMEC as a Senior Researcher and R&D Team Leader, where he is leading to the activities on Analog Integrated Circuit design for portable and implantable biomedical applications. During his research on analog integrated circuit design, he has (co)authored over 40 publications, 3 book chapters, and a book on ultra-low-power circuit and system design for biomedical applications.

He is also the (co-) recipient of the best paper award at Smart System Integration Conference, and "Sensors & Transducers Journal: 10 Best Articles Published in 2008" award. Dr. Yazicioglu is a member of IEEE and also serves in the Technical Program Committee of European Solid State Circuits Conference (ESSCIRC).



Bernard Grundlehner received the M.Sc. degree in electrical engineering in 2001 from the University of Twente. He worked as a researcher on improvement of audio and speech playback from 2002 until 2007. In 2007, he joined imec as a researcher on biomedical signal processing, working on affective computing and EEG signal processing. His current research interests include statistical pattern recognition, neuroscience and bio-acoustics.



Pieter Harpe received the M.Sc. and Ph.D. degrees from the Eindhoven University of Technology, The Netherlands. In 2008, he started as researcher at Holst Centre/imec, The Netherlands. Since then, he has been working on ultra low-power wireless transceivers, with a main focus on ADC research and design. In April 2011, he joined Eindhoven University of Technology as assistant professor on low-power mixed-signal circuits.



Kofi A. A. Makinwa (M'97–SM'05–F'11) received the B.Sc. and M.Sc. degrees from Obafemi Awolowo University, Nigeria, in 1985 and 1988, respectively. In 1989, he received the M.E.E. degree from the Philips International Institute, The Netherlands, and in 2004, the Ph.D. degree from Delft University of Technology, The Netherlands.

From 1989 to 1999, he was a Research Scientist with Philips Research Laboratories, Eindhoven, The Netherlands, where he worked on interactive displays and on front-ends for optical and magnetic recording systems. In 1999,

he joined Delft University of Technology, where he is now an Antoni van Leeuwenhoek Professor in the Faculty of Electrical Engineering, Computer Science and Mathematics. His main research interests are in the design of precision analog circuitry, sigma-delta modulators, smart sensors and sensor interfaces. This has resulted in one book, 14 patents, and over 140 technical papers.

Kofi Makinwa is on the program committees of several international conferences, including the European Solid-State Circuits Conference (ESSCIRC) and the IEEE International Solid-State Circuits Conference (ISSCC). He has also served as a guest editor of the Journal of Solid-State Circuits (JSSC). He is the co-recipient of several best paper awards, from the JSSC, ISSCC, Transducers and ESSCIRC among others. In 2005, he received a

Veni Award from the Netherlands Organization for Scientific Research and the Simon Stevin Gezel Award from the Dutch Technology Foundation. He is a distinguished lecturer of the IEEE Solid-State Circuits Society, a fellow of the IEEE, and a fellow of the Young Academy of the Royal Netherlands Academy of Arts and Sciences.



Chris Van Hoof (M'91) is Director of Integrated Systems at IMEC in Leuven and Program Director of HUMAN++ at imec in Leuven and the Holst Centre in Eindhoven, the Netherlands. He received a Ph.D. in Electrical Engineering from the University of Leuven in 1992. Chris Van Hoof has a track record of 20 years of initiating, executing and leading national and international contract R&D. He transferred technology to one startup and delivered space qualified flight hardware to two cornerstone European Space Agency missions.

He has more than 500 publications and has given over 40 invited/plenary talks. Since 2000, Chris Van Hoof has also been part-time professor at the University of Leuven (K.U. Leuven), in charge of courses on Integrated Systems and Design for micro-and nanoelectronics. From 2011 onwards, he is appointed as full professor.